Morphology-Dependent Energy Transfer Dynamics in Fluorene-Based Amphiphile Nanoparticles

Amy L. Stevens,[†] Adrien Kaeser,[‡] Albertus P. H. J. Schenning,[‡] and Laura M. Herz[†,*]

[†]Department of Physics, University of Oxford, Clarendon Laboratory, Parks Road, Oxford OX1 3PU, United Kingdom and [‡]Laboratory for Functional Organic Materials and Devices, Eindhoven University of Technology, P.O. Box 513, 5600 MB Eindhoven, The Netherlands

ABSTRACT

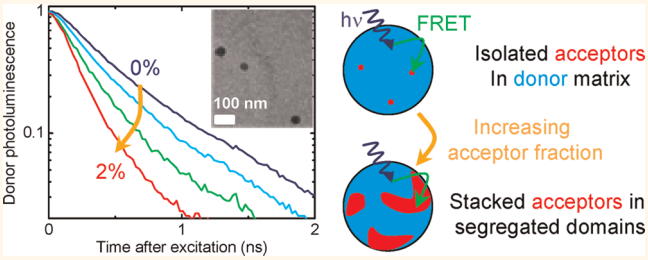

Nanoparticles are interesting systems to study because of their large range of potential uses in biological imaging and sensing. We investigated molecular nanoparticles formed by fast injection of a small volume of molecularly dissolved fluorene-derivative amphiphilic molecules into a polar solvent, which resulted in solid spherical particles of ~80 nm diameter with high stability. Energy transfer studies were carried out on two-component nanoparticles that contained mixtures of donor and acceptor amphiphiles of various fractions. We conducted time-resolved photoluminescence measurements on the two-component nanoparticles in order to determine whether the fundamental donor–acceptor interaction parameter (the Förster radius) depends on the acceptor concentration. The Förster radius was found to be large for very low incorporated acceptor fractions (<0.1%), but it declined with increasing concentration. These changes were concomitant with shifts in the acceptor emission and absorption circular dichroism spectra that indicated an increasing clustering of acceptors into domains as their fraction was raised. In addition, for acceptor fractions below 2% the extracted Förster radii were found to be significantly larger than predicted from donor–acceptor spectral overlap calculations, in accordance with efficient excitation diffusion within the donor matrix, aiding the overall transfer to acceptors. We conclude that energy transfer in two-component nanoparticles shows a complex interplay between phase segregation of the constituent donor and acceptor molecules and excitation diffusion within their domains.

KEYWORDS: nanoparticles · amphiphile · self-assembly · π-conjugated molecules · morphology

Fluorescent nanoparticles are becoming more and more central to biological imaging and sensing applications. In particular, nanoparticles composed of organic polymer chains or self-assembled molecular aggregates[1] have several key advantages over inorganic semiconductor quantum dots or conventional probes. For example, molecular nanoparticles are not cytotoxic[2,3] and do not impair a cell's functionality.[4,5] If molecular packing is controlled carefully, enhanced emission, rather than quenching, is observed in high concentrations of oligomeric fluorophore nanoparticles.[1,6] Importantly, polymeric nanoparticles have large multiphoton cross sections[5,7,8] and are several orders of magnitude brighter than conventional fluorescent dyes and quantum dots[9] when imaged using popular bioimaging techniques such as multiphoton fluorescence microscopy. Molecular nanoparticles have been successfully used to target, track,[8,10] and image specific biomolecules.[5] For example, polymer-loaded surfactant nanoparticles were functionalized with folic acid to selectively target and image cancer cells.[11] Utilized as sensors, the nanoparticles capture the state of the cellular environment, yielding, for example, pH[12] or oxygen levels.[3] The molecular approach is particularly attractive here, as it allows nanoparticles of tens to hundreds of nanometers[2,11] in diameter to be made, whose properties can be tailored through molecular design and its impact on particle assembly. Clever control of intermolecular interactions has been critical in this context, with $\pi-\pi$ or van der Waals interactions, hydrophobic effects,[1] the ratio of hydrophobic to hydrophilic parts of the molecule,[13] the side chain and tail architecture,[6,14,15] and the concentration of molecules present[16] all playing a critical role.

Energy transfer within such nanoparticles has proven to be a particularly powerful approach toward enhancing the sensitivity of a nanoparticle to particular environmental parameters. For example, such donor–acceptor composite nanoparticle systems have been used to dramatically amplify emission color shifts upon changes in aqueous pH[17] or the concentration of oxygen.[3] Förster's theory[18–21] of resonant energy transfer (FRET) occurring between energy donating and accepting point dipole transition

* Address correspondence to l.herz1@physics.ox.ac.uk.

Received for review December 18, 2011 and accepted May 1, 2012.

Published online May 01, 2012
10.1021/nn204942r

moments has recently been applied to these composite nanoparticles.[17,22] The rate at which FRET occurs is predicted to be proportional to $(R_0/R)^6$, where the Förster radius R_0 is the critical transfer distance for which excitation transfer and spontaneous donor deactivation are of equal probability.[19,23] The strong dependence of the transfer rates on the donor–acceptor separation R means that energy transfer processes will depend not only on the spectral characteristics of the donor–acceptor pair but also critically on their organization.[24,25]

In the study presented here, we have investigated the influence of molecular arrangement on the energy transfer in donor–acceptor composite nanoparticles. Stable, solid nanoparticles of ~80 nm diameter were produced using a fast injection method of amphiphile molecules dissolved in THF into a larger volume of water. We utilized time-resolved photoluminescence measurements to probe the energy transfer dynamics in two-component nanoparticles containing mixtures of donors and acceptors of various fractions. We find that at low incorporated acceptor fractions (<0.1%) energy transfer is surprisingly efficient compared to theoretical expectations from donor–acceptor emission resonance calculations. Our results suggest that at such low acceptor fractions efficient excitation diffusion within the donor matrix allows an enhancement of the overall transfer rate to acceptors. However, at higher incorporated acceptor fractions, the energy transfer efficiency declines concomitant with changes occurring in emission and circular dichroism spectra of the acceptor molecules that are indicative of acceptor clustering into domains. Such phase segregation appears to be driven by relatively small changes between the donor and acceptor molecules, *e.g.*, in the torsion angle of the central fluorescing moiety, and is therefore likely to be of high relevance to a wide variety of organic nanoparticle systems. While acceptor phase segregation is found to be detrimental to energy transfer efficiencies within the nanoparticle, it offers opportunities for use in biosensing, *e.g.*, by opening a facile route to high-affinity targeting of biomolecules with multiple adsorption sites. Our results demonstrate that optimization of energy transfer in two-component nanoparticles requires not only excellent spectral resonance between the chromophore pair but also careful control over phase segregation of the constituent donor and acceptor molecules and of excitation diffusion within their domains. These findings impact the design of molecules for fluorescent organic nanoparticles and their supramolecular assembly, which is strongly linked to their efficiency as biomolecular probes.

RESULTS AND DISCUSSION

The fluorescent nanoparticles under investigation were composed of amphiphile co-oligomers incorporating either an electron-rich naphthalene or an electron-withdrawing benzothiadiazole unit[7,26] between two fluorene units. Figure 1 shows chemical structures and schematic depictions of the respective amphiphiles AMP1-N (naphthalene derivative) and AMP1-B (benzothiadiazole derivative). Chiral branched alkane side chains are attached to the fluorenes to prevent photooxidation to 9-fluorenone,[27,28] to probe self-assembly by circular dichroism, and to enhance solubility in organic solvents, while hydrophilic ethylene glycol and hydrophobic alkane chains on opposite ends impose amphiphilic character. Details of the chemical synthesis and full characterization of AMP1-N and AMP1-B are provided in the Supporting Information.

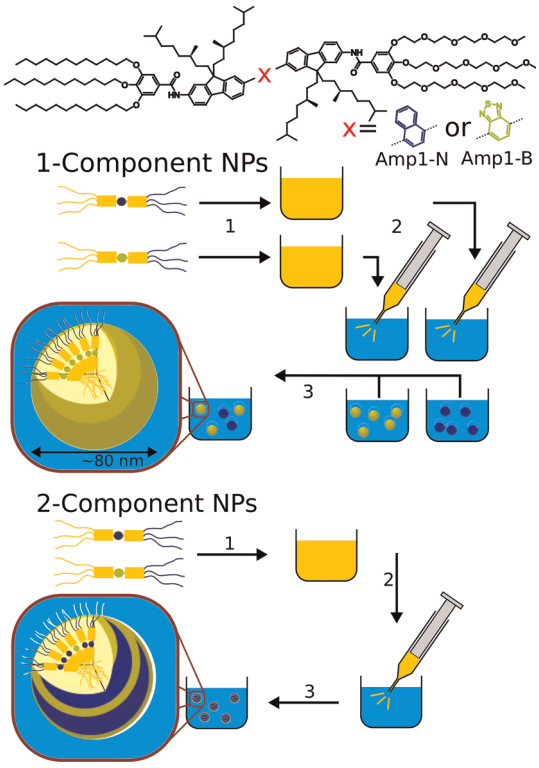

Figure 1. (Top) Chemical structure and schematic representations of fluorene-based amphiphiles AMP1-N and AMP1-B. An electron-rich naphthalene (depicted as a blue disk) or an electron-withdrawing benzothiadiazole (green disk) unit is covalently bonded between two fluorenes (orange squares) with hydrophilic ethylene glycol wedges (blue strands) and hydrophobic alkoxy wedges (yellow strands) attached to either end, and chiral side chains. (Bottom) Preparation of single-component nanoparticles. Stock solutions in THF of either AMP1-N *or* AMP1-B are injected into water, upon which stable nanoparticles containing just one molecular species form. Preparation of two-component nanoparticles: stock blend solutions of AMP1-N *and* AMP1-B are injected into water, creating mixed nanoparticles composed of both molecules.

Nanoparticles were formed through self-assembly by the fast injection method,[29,30] as indicated in the schematic shown in Figure 1. Amphiphile molecules were molecularly dissolved in THF (1 mM), of which a small volume (15 μL) was injected into a large excess (5 mL) of ultrapure water; full details are given in the Materials and Methods section below. Single-component

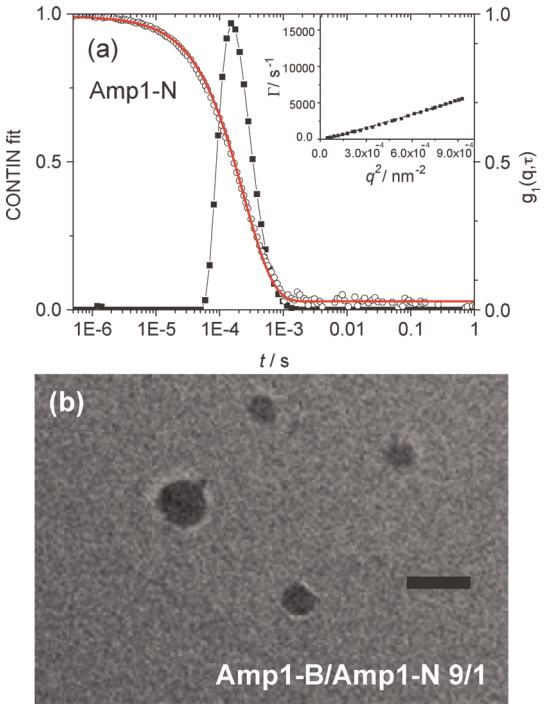

Figure 2. Examples of nanoparticle characterization data. (a) Multiangle dynamic light scattering (DLS) data for AMP1-N nanoparticles. A hydrodynamic radius of 40.8 ± 0.4 nm was extracted from CONTIN fits of the 150° correlation function and single-exponential fits of angular data (see inset). (b) Transmission electron microscopy (TEM) image of AMP1-B/AMP1-N two-component nanoparticles with mixing ratio 9:1 (*i.e.*, 90% acceptor concentration). The scale bar represents 200 nm. It should be noted that in dry TEM the deposited particles flatten out on the surface.

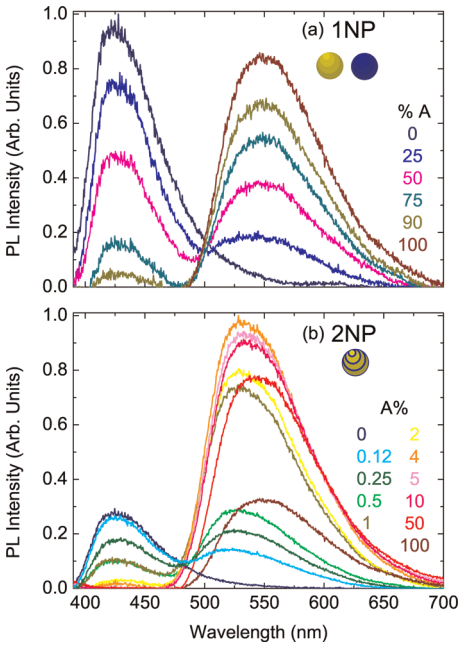

Figure 3. Time-integrated photoluminescence spectra of (a) blends of single-component nanoparticles (1NP) for which each nanoparticle contains either just AMP1-N or just AMP1-B molecules and (b) two-component nanoparticles (2NP) for which each particle contains a blend of the two molecules. Spectra are shown for a range of different percentages of AMP1-B acceptor molecules present. All samples were excited at a wavelength of 375 nm, for which the ratio of the molar extinction coefficient of the donor to that of the acceptor molecule was 2.6:1 (see Supporting Information).

(1NP) or two-component (2NP) nanoparticles were made by incorporating either just a single molecular species or a blend of AMP1-N and AMP1-B in the THF solution prior to injection (see Figure 1). Once formed, nanoparticles were found to be stable, showing negligible exchange of molecules over a time period of two days (*vide infra*).

Comprehensive characterization of the nanoparticles was carried out using transmission electron microscopy (TEM), multiangle light scattering (DLS), and small-angle X-ray scattering (SAXS) techniques. Figure 2 and Figure SI-5 show examples for AMP1-N, mixed AMP1-B/AMP1-N, and AMP1-B nanoparticles, respectively. DLS and SAXS measurements indicate the presence of spherical nanoparticles with 80 nm diameter in solution. These results are in agreement with the size distributions displayed in TEM images, which also show that these nanoparticles are solid spheres, rather than vesicles (see Figure 2 and Supporting Information). Changes in the absorption spectra of AMP1-N and AMP1-B following injection are characteristic of H-aggregate formation and general molecular stacking (see Figure SI-4, Supporting Information, and ref 13). We find a relatively weak bisignate Cotton effect in the circular dichroism measurements (see Figure SI-6, Supporting Information), indicating that helical domains form within the nanoparticles. Overall, the combined set of characterization data suggests that the nanoparticles are best described as spherical molecular solids with a low degree of internal ordering. All measurements presented here were conducted on freshly made samples, *i.e.*, no postformation treatments applied, since annealing conjugated oligomer solids may change their organization[13,14] and affect their electronic properties.[31]

Since good spectral overlap exists between the emission spectrum of AMP1-N (see Figure 3) and the absorption spectrum of AMP1-B (Supporting Information), the former should act as energy donor and the latter as acceptor in mixed nanoparticles.[30,32] In order to investigate such energy transfer dynamics, we conducted time-integrated photoluminescence (TIPL) and time-correlated single-photon counting (TCSPC) measurements on nanoparticles in solution at room temperature. Figure 3a displays time-integrated photoluminescence spectra for blends of single-component nanoparticle (1NP) samples for which each nanoparticle contains either just AMP1-N or just AMP1-B molecules. The AMP1-N donor emission is found to peak at 425 nm, while AMP1-B acceptor molecules emit broadly around 550 nm, in agreement with previous literature reports on related molecules.[27,30,32−35] As the overall acceptor fraction in the sample increases, the

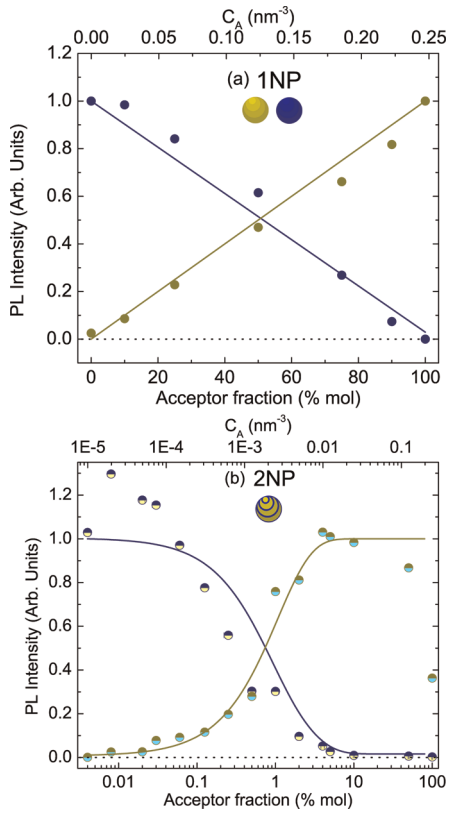

Figure 4. Normalized time-integrated photoluminescence intensities of the AMP1-N donor (blue disks) and AMP1-B acceptor (yellow disks) emission wavelengths as a function of acceptor mole fraction for (a) blends of single-component nanoparticles (1NP) and (b) two-component nanoparticles (2NP). For 2NP particles, the acceptor emission was determined through spectral integration after subtraction of the donor emission in order to account for the observed peak shifts (see Figure 3). For all other cases, the peak donor and acceptor emission intensities at 430 and 575 nm, respectively, were taken. The top axis also shows the acceptor concentration (C_A) deduced from the acceptor mole fraction through assumption of a density of 1 g cm^{-3} within the nanoparticle. The solid lines are fits to the data based on (a) the assumption of a linear superposition of donor and acceptor emissions and (b) the results of Förster theory assuming a random distribution of acceptor molecules within the two-component nanoparticles, as discussed in the text.

donor emission decreases with a corresponding acceptor emission increase. The spectra appear to be a linear superposition of separate donor and acceptor emissions with an isosbestic point at 500 nm and no apparent peak shifts. To illustrate this more quantitatively, the PL emitted from the donor and acceptor molecules is plotted in Figure 4a as a function of the percentage of acceptors present in the sample. The normalized data can be fitted with linear relationships that show a crossover at an acceptor fraction of 50%. These results demonstrate an absence of energy transfer processes from AMP1-N to AMP1-B nanoparticles in accordance with the low concentration of NPs in water[33,36] (3 μM). They also suggest that over the time window of observation (two days) nanoparticles are stable; that is, they do not exchange their constituent molecules between one another.

For two-component nanoparticles (2NP), each composed of a blend of AMP1-N and AMP1-B, the spectral evolution with acceptor concentration is drastically different. Figure 3b shows that for 2NP the donor emission rapidly reduces in intensity upon introduction of acceptor until, at an acceptor fraction of 2%, it can no longer be detected. The observed general enhancement of acceptor emission and quenching of donor emission is strongly indicative of efficient intrananoparticle energy transfer. However, the evolution of the acceptor (AMP1-B) emission spectra with increasing acceptor fraction is somewhat more complex: at low acceptor fractions (<0.5%), the acceptor emission peaks at 520 nm, which gradually shifts to about 545 nm with increasing acceptor concentration. In addition, the acceptor emission intensity first increases steeply with acceptor concentration, but then peaks at 4% and gradually declines for larger incorporated fractions. When the intensity of the donor emission is plotted against the acceptor concentration (see Supporting Information), the observed nonlinear dependence reveals that a description in terms of simple static or dynamic quenching models is inappropriate here. These trends reflect morphological changes in the blended nanoparticles, which will be discussed in more detail further below.

Figure 4b shows the integrated donor and acceptor emission intensities as a function of acceptor mole fraction. Crossover between relative donor and acceptor emissions now occurs at an incorporated acceptor fraction of only ~0.7%, as a result of efficient intraparticle energy transfer. As a first approximation, these results can be modeled within Förster theory, which predicts the fraction of photons emitted from the donor (ϕ_D) and the acceptor (ϕ_A) to be[18]

$$\begin{aligned} \phi_D(X) &= \Phi_D(1 - [\sqrt{\pi}Xe^{X^2}(1 - \mathrm{erf}(X))]) \\ \phi_A(X) &= \Phi_A(\sqrt{\pi}Xe^{X^2}(1 - \mathrm{erf}(X))) \end{aligned} \quad (1)$$

Here, Φ_D and Φ_A are the radiative efficiencies of the donors (in the absence of acceptors) and acceptors (in the absence of donors), *i.e.*, within homogeneous nanoparticles of 100% AMP1-N or AMP1-B, respectively, erf is the error function, and $X = 2/3((\pi)^{1/2})^3 R_0^3 C_A$ gives a measure proportional to the number of acceptor molecules contained in the "interaction volume" spanned by the Förster radius R_0.[18,23] This model assumes that a random three-dimensional distribution of donor and acceptor chromophores is present and that the distance between the interacting chromophores is sufficiently large in order for their oscillating moments to be approximated as point dipoles. Typical Förster radii and exciton diffusion lengths in disordered organic solids have been found to be of the order of a few nanometers[23,33,37] (although fluorescence blinking can occur in polymer nanoparticles of a few tens of nanometers in size,[38,39] and exciton diffusion may range even further for highly ordered, coupled *J*-aggregates such as those occurring

in cyanines[40,41]). The disordered molecular nanoparticles under investigation here have a diameter (80 nm) much larger than such excitation transfer lengths, and it therefore seems appropriate to model the energy transfer within the nanoparticle using the above equations. However, this model may not be fully appropriate for very large acceptor concentrations, for which donor–acceptor separation may become smaller than the size of the photoexcitations. Figure 4b shows the curves obtained by simultaneously fitting scaled versions of eqs 1 to the normalized PL emission intensities of the donor and acceptor. For these fits, the acceptor concentration C_A was deduced from the acceptor mole fraction through assumption of a density within the nanoparticle of 1 g cm^{-3} as a typical value for molecular solids.[42] Assuming a concentration-independent Förster radius, we obtain a value of $R_0 = 3.97 \pm 0.03$ nm through this procedure. It should be pointed out that the fitting is most sensitive to the crossover point around an incorporated acceptor fraction of ~0.7%, and this method is therefore particularly representative of the interaction strength around this concentration.

In addition, we may obtain information of the Förster radius expected for the AMP1-N and AMP1-B molecular system by considering the spectral overlap between donor emission and acceptor absorption. From the conditions of electronic resonance, the Förster radius can be evaluated as[19,43]

$$R_0 = \left[\frac{9000 \ln 10}{128\pi^5} \frac{\kappa^2 \phi_D}{n^4 N} \int_0^\infty \frac{1}{\bar{\nu}^4} f_D(\bar{\nu})\, \varepsilon_A(\bar{\nu})\, d\bar{\nu}\right]^{1/6} \quad (2)$$

Here, κ^2 is the dipole orientation factor, $\phi_D = 0.4$ is the fluorescence quantum yield of the donor in the absence of energy transfer, n is the refractive index of the material at the peak of the integrand, N is Avogadro's constant, $f_D(\bar{\nu})$ is the fluorescence spectrum of the donor NP (Figure 3b) with integrated intensity normalized to unity on a wavenumber scale, and $\varepsilon_A(\bar{\nu})$ is the molar decadic extinction coefficient of the acceptor (Figure SI-6a in the Supporting Information). As a reasonable approximation, we assume that the nanoparticles resemble an amorphous polymer film with refractive index of 1.5[42,44] within the vicinity of the interaction volume. We choose $\kappa^2 = 0.48$ in accordance with the presence of random but fixed interacting dipoles.[45,46] Inserting these parameters into eq 2, we obtain a Förster radius for energy transfer between AMP1-N donors and AMP1-B acceptors of 2.9 nm and for homotransfer of energy from one AMP1-N to another AMP1-N molecule of 1.5 nm. The value of $R_0 = 2.9$ nm is significantly lower than that experimentally derived from the concentration quenching experiments discussed above (3.97 nm). This discrepancy is most likely the result of exciton diffusion within the AMP1-N donor matrix prior to energy transfer,[22] made possible by the large homotransfer rates between AMP1-N molecules. Such exciton-diffusion-aided energy transfer is well known to occur in dye-doped thin films of conjugated polymer solids[47–49] and highly ordered J-aggregates.[40,41] These results are also in agreement with those for other NP systems, for which the observation of greatly enhanced acceptor emission for small incorporated amounts[25,33,50–53] has led to the conclusion that each acceptor effectively quenches a large number of donor sites.[17,33]

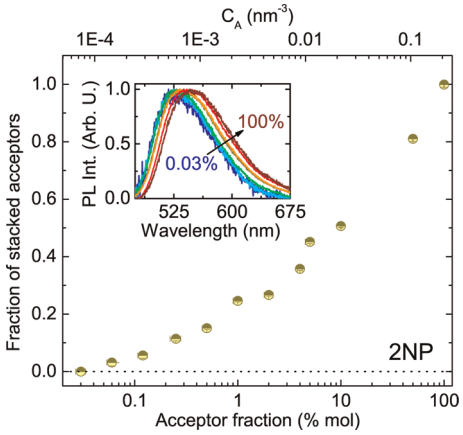

Figure 5. Fraction of AMP1-B acceptor emission from two-component nanoparticles attributable to phase-segregated, stacked absorber domains, plotted as a function of acceptor percentage and acceptor concentration. The inset shows the normalized AMP1-B acceptor emission from two-component nanoparticles after the AMP1-N emission had been numerically removed. The normalized spectra were then fitted with a sum of emission spectra from "stacked" acceptors and "unstacked" acceptors from which the fraction originating from stacked acceptors was extracted, as shown.

The above assumption that acceptors are randomly distributed within a nanoparticle donor matrix needs to be reconsidered to some extent, because of the observed shifts in acceptor emission spectra with incorporated acceptor fraction (see Figure 3b). To analyze these shifts, the emission from the AMP1-B acceptor molecules within the two-component nanoparticles was isolated by numerically removing the emission from the AMP1-N donor. To this end, the emission from AMP1-N one-component nanoparticles was scaled to the peak of the AMP1-N emission in two-component nanoparticles and subtracted. The remaining AMP1-B acceptor emission was normalized and is shown in the inset of Figure 5: a clear red-shift is evident as the acceptor concentration is increased. These changes can be attributed to phase segregation of AMP1-B into homogeneous domains at high incorporated fraction. While at low acceptor concentrations, acceptors are uniformly distributed in the donor nanoparticle matrix, at high acceptor fractions, the pronounced red-shift and PL intensity decrease with increasing acceptor concentration (Figure 3b), suggesting that low-energy, weakly fluorescent aggregates form.[2,11,22,31,50,52,54–58] Molecular mechanics calculations on molecules identical to AMP1-N and AMP1-B

(apart from both ends being terminated with alkyl chains) have indicated that the torsion angle between the fluorene and the central aromatic moieties is 71° for the former, but only 40° for the latter.[32] These differences in molecular planarity were shown to induce strong differences in aggregation behavior for homogeneous aggregates.[32] From the analysis of the PL emission spectra shown in Figure 5 it thus appears that differences in planarity between the two molecules can also be a driver of substantial phase segregation in mixed nanoparticles of aggregated molecules. To quantify these changes with nanoparticle composition, we consider the acceptor emission to be a linear superposition of the spectrum for AMP1-B within an AMP1-B domain and the spectrum for AMP1-B isolated in an AMP1-N matrix. The normalized acceptor emission spectra for various acceptor fractions (inset in Figure 5) were thus fitted with the sum of the acceptor spectrum for 100% fraction (scaled with A_1) and that for 0.03% (scaled with A_2), with A_1 and A_2 being the fitting variables. The fractional contribution to the AMP1-B emission originating from stacked AMP1-B domains is then given by $A_1/(A_1 + A_2)$, which is plotted in Figure 5 as a function of acceptor concentration. These values show a clear trend toward acceptor stacking and morphological phase segregation within the nanoparticles as the acceptor concentration is increased. Circular dichroism measurements support these observations: a bisignate Cotton effect in the acceptor absorption region rises in amplitude once the acceptor fraction incorporated within the two-component nanoparticles exceeds a few percent (see Supporting Information), in agreement with formation of domains with some degree of helical local ordering.

Since the nanoparticles undergo morphological changes with composition, it is interesting to investigate how the energy transfer within the nanoparticles is affected as a result. For this purpose, we time-resolved the donor and acceptor emission from the nanoparticles in order to extract transfer efficiencies from these data as a function of acceptor concentration. Figure 6 shows the donor emission decay as a function of time after excitation for one-component nanoparticle (1NP) blends and two-component (2NP) nanoparticles. The corresponding curves measured at the acceptor emission peak (see Supporting Information) are complicated by contributions from overlapping donor emission. Therefore, in the following, we focus on analysis of the PL dynamics recorded at the donor emission peak, which are clearly separable from the acceptor emission. The donor decay transients are close to monoexponential for donor-only nanoparticles (Figure 6a) but deviate significantly from such behavior for two-component nanoparticles (Figure 6b). As a general guide, we extracted the time τ taken for the emission to decay to $1/e$ of its initial value and plotted these values as a function of concentration in the insets of

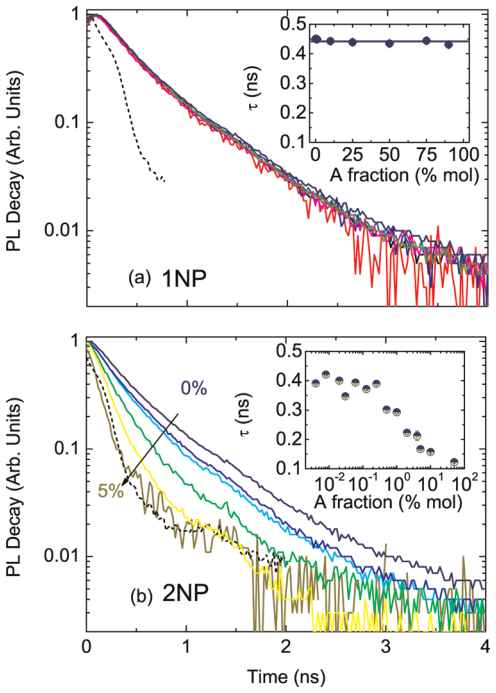

Figure 6. Normalized time-resolved photoluminescence decays for (a) single-component nanoparticle (1NP) blends and (b) two-component nanoparticles (2NP) measured at the AMP1-N donor emission peak wavelength (430 nm). The fractions of acceptor in the 1NP samples are 0, 1, 10, 25, 50, 75, and 90% and in the 2NP samples are 0, 0.02, 0.12, 1, 2, and 5%. The dashed curves represent the instrument response function. The insets show the time τ taken for the donor emission to decay to $1/e$ of its initial value, extracted by fitting a monoexponential function ($y = Ae^{(-t/\tau)}$) to these decay data within a range starting at the peak and finishing 1.0 ns after the peak. The blue line in the inset of (a) indicates the average of the AMP1-N emission lifetimes for the single-component nanoparticle blends.

Figure 6. For one-component nanoparticle blends the donor emission has a lifetime of ~0.44 ns independent of the acceptor concentration present in the sample, indicating the absence of energy transfer. These results thus illustrate again that once separate one-component nanoparticles comprising either AMP1-B or AMP1-N have formed, blends of these nanoparticles are stable and do not exchange excitation energy in dilute solution. For two-component nanoparticles, on the other hand, AMP1-N donor emission decays, shown in Figure 6b, become faster as the AMP1-B acceptor percentage inside them increases in accordance with efficient energy transfer[22,50,51] occurring even at low incorporated acceptor fraction. These effects are reflected by the extracted $1/e$ donor emission decay times, which decrease sharply at acceptor fractions above ~0.1% until the decay traces approach the instrument response function at ~5%, above which no further change can be resolved.

To analyze the energy transfer dynamics for the two-component nanoparticles, we divided the donor emission curves shown in Figure 6b by the single-component donor nanoparticle emission (*i.e.*, containing 0% acceptor).

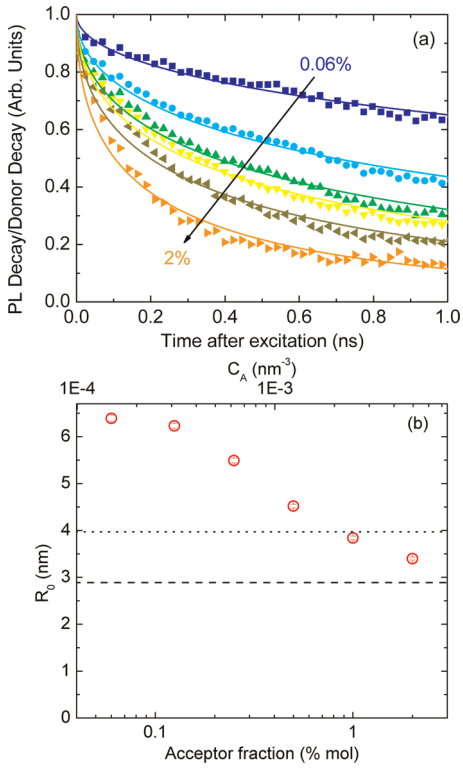

Figure 7. (a) Normalized time-resolved decay of the photoluminescence from AMP1-N donors within two-component nanoparticles (2NP) divided by the decay curve obtained for one-component AMP1-N nanoparticles (*i.e.*, containing 0% acceptor). Curves are shown for acceptor concentrations of 0.06, 0.12, 0.25, 0.5, 1, and 2%. The detection wavelength was set to the donor photoluminescence emission peak wavelength (430 nm). The solid lines are fits to the data based on a three-dimensional Förster model, as described in the text. (b) Förster radius (R_0) extracted from the fits to data shown in (a), plotted as a function of acceptor percentage (bottom axis) and acceptor concentration (top axis). The dashed line shows the Förster radius of 2.9 nm expected from the spectral overlaps of donor emission and acceptor absorption according to eq 2. The dotted line represents the Förster radius of 3.97 ± 0.03 nm, extracted from fits of eqs 1 to the time-integrated photoluminescence intensities at the donor and acceptor emission wavelengths shown in Figure 4 under the assumption of randomly distributed acceptors within the nanoparticles.

Through this method we obtain the AMP1-N donor emission decay component that is solely attributable to energy transfer to AMP1-B acceptor molecules.[49] The resulting energy transfer transients (shown in Figure 7a) are again nonexponential and strongly dependent on acceptor concentration, both of which are expected from Förster theory.[18] Because of the dependence of the Förster energy transfer rate on the donor−acceptor separation to the inverse power of six,[19] excited donors located close to the acceptor will transfer their energy first. As a result, energy transfer within the ensemble appears to slow with time until at long times only those donors located far from acceptors emit, for which recombination effectively competes with energy transfer to acceptors.[59] As a result, the exact shape of curves depends strongly on the geometric arrangement of the donor−acceptor ensemble. For spatially random distributions of donor−acceptor ensembles, the energy transfer dynamics are predicted to follow stretched exponentials whose exponent α depends on the dimensionality of the system.[43,46,60] Our analysis of the shape of the donor decay curves (see Supporting Information) accordingly demonstrates that for acceptor concentrations lower than 1% the system can be well-approximated by a random distribution of donor and acceptor pairs in three dimensions. This suggests that for relatively low levels of acceptor phase segregation and for nanoparticle dimensions much larger than the Förster radius, the Förster model for three-dimensional molecular materials can be applied to the two-component nanoparticle system. However, for concentrations exceeding ~1%, significant deviation occurs from that expected for three-dimensional random solids (see Supporting Information), in agreement with the changes in the acceptor emission (see Figure 5) observed beyond these concentrations. Taken together these results strongly suggest that acceptor domains form in the two-component nanoparticle, which increase in size with increasing acceptor concentration until significant deviations from energy transfer models based on random distributions become apparent.

For the regime of low acceptor concentration, we therefore apply the three-dimensional Förster model for evenly distributed acceptors in order to extract the Förster radius (R_0) from the energy transfer transients shown in Figure 7a. Here, the donor emission transients, $I_{DA}(t)$, attributable to energy transfer are given by[18,23,59]

$$I_{DA} = A \exp\left(-\frac{4}{3}\sqrt{\pi^3} C_A R_0^3 \sqrt{\frac{t}{\tau_D}}\right) \qquad (3)$$

where A is a scaling constant and τ_D = 0.45 ns is the donor decay lifetime in the absence of acceptors. Figure 7b displays the Förster radii (R_0) extracted from the fits (shown as solid lines in Figure 7a) as a function of acceptor concentration C_A. In addition, values for R_0 calculated from spectral overlaps (2.9 nm, dashed line) and changes in the TIPL spectra with C_A (3.97 nm, dotted line) are indicated. The Förster radius extracted from the time-resolved data crosses the value determined from the TIPL spectra at an acceptor fraction of ~0.7%. This makes sense, as the determination of energy transfer efficiencies from time-integrated spectra is mainly sensitive to the region in which strong changes with acceptor fraction occur, which happens to be around 0.7% for these nanoparticles; see Figure 4b.

The Förster radii extracted from time-resolved data show a strong dependence on the acceptor fraction incorporated in the nanoparticles. For small acceptor fractions (<0.1% mol) very large values of R_0 are found, which decline rapidly as the acceptor fraction increases to 2%. At all concentrations within this range, values

larger than those predicted from spectral overlap calculations are observed. There are at least three plausible reasons for the observed behavior, two of which relate to morphological changes occurring in the nanoparticles with compositional changes. First, morphological effects arise from stacking of acceptors into domains with increasing acceptor incorporation. Our analysis of the acceptor emission and circular dichroism spectra (see Figure 5 and Figure SI-6 in the Supporting Information) suggests that acceptor clustering increases slowly below acceptor fractions of ~1% in the nanoparticles and much more rapidly for larger fractions. Such phase segregation will lead to larger average donor−acceptor distances (compared to uniform distributions), which may be modeled as effective reductions in acceptor concentrations for low included fractions. As a result, we observe a sharp decline of the Förster radius with increasing acceptor fraction in the nanoparticles. Second, the inclusion of very small acceptor fractions into the nanoparticles may to some extent disrupt the partially ordered donor domains present in donor-only nanoparticles. Such changes in packing may affect both the radiative decay rate (through dipole coupling between chains in close proximity[55]) and the nonradiative decay rate (through the effect of molecular flattening on intersystem crossing rates[61]). Comparison of emission and absorption spectra for AMP1-N in molecularly dissolved, freshly aggregated, and annealed aggregated form suggests that both mechanisms influence decay rates in AMP1-N nanoparticles.[13] Such influence of molecular packing on the internal de-excitation pathways in the donor will also affect the overall energy transfer to the acceptor, as this is a competing process. Because energy transfer in mixed nanoparticles has to be referenced against donor de-excitation in 100%-donor nanoparticles, subtle morphological effects may lead to values extracted for the Förster radii that could be artificially increased or decreased to some extent. Finally, it should be noted that the Förster radii extracted for the acceptor fraction range of 0.05−2% are always larger than the value expected from spectral overlap calculations. This is most likely because Förster's original model as applied to our data neglects the effect of excitation diffusion within the nanoparticles, which is caused by homoenergy transfer between donor molecules. We reported above that the Förster radius calculated from spectral overlaps for such homo energy transfer is 1.5 nm; hence efficient exciton diffusion within donor domains should be expected. Such diffusion increases the energy transfer rate by repopulating de-excited donors near acceptors with excitons.[47,49,62] Hence, we observe the experimentally extracted Förster radii, both from time-integrated PL intensities and from PL decays, to be larger than the Förster radius expected from pure spectral overlaps. Our results are in agreement with those by Wu *et al.*, who found that the Förster energy transfer efficiencies in a dye-doped polyfluorene nanoparticle system could be modeled correctly only with Monte Carlo-type simulations that included exciton diffusion.[22]

CONCLUSIONS

We have investigated fluorescent nanoparticles self-assembled from amphiphile fluorene-based molecules AMP1-N and AMP1-B in which the former may act as an excitation donor and the latter as an acceptor. Nanoparticles of ~80 nm were found to form following a fast injection method of amphiphiles dissolved in THF into a larger volume of water. These nanoparticles were shown to be stable over time scales of at least days: when single-component nanoparticles containing solely AMP1-N were mixed with those containing solely AMP1-B, no energy transfer was observed, indicating the absence of molecular exchange between the particles.

Energy transfer studies were subsequently carried out through time-resolved PL measurements on two-component nanoparticles that contained mixtures of AMP1-N donor and AMP1-B acceptor of various fractions. The fundamental donor−acceptor interaction parameter (the Förster radius) was found to be large for very low incorporated acceptor fractions (<0.1%), but it declined with increasing concentration. These changes were concomitant with shifts in the acceptor emission and absorption circular dichroism spectra that indicated an increased clustering into domains as the acceptor fraction was raised. In addition, for acceptor fractions below 2% the extracted Förster radii were found to be significantly larger than that predicted from spectral overlap of the donor emission with the acceptor absorption. Efficient exciton diffusion resulting from donor−donor energy transfer is therefore also likely to make a significant contribution to the overall energy transfer from donors to acceptors.

In summary, energy transfer in the two-component nanoparticles was shown to depend on a complex interplay between phase segregation of the constituent donor and acceptor molecules and excitation diffusion within their domains. Such transfer appears to be particularly efficient for very low incorporated acceptor fractions, for which acceptors are evenly dispersed in a donor matrix, which aids the overall energy transfer by offering effective exciton diffusion pathways. These results are in agreement with those for other nanoparticle systems for which the observation of greatly enhanced acceptor emission under small incorporated amounts[25,33,50−52] informs the conclusion that each acceptor quenches a surprisingly large number of surrounding donors.[17,33] Energy transfer processes are important in nanoparticles, as they may be used for example to amplify detection sensitivities to particular molecules such as oxygen.[3] We demonstrate here that the morphology of the molecules in the

NP system has a clear impact on such energy transfer efficiencies. When nanoparticles are used to track and image biomolecules or to sense chemical compounds, such effects are important, as they determine the fluorescence intensities and therefore operational sensitivities of the nanoparticles.

MATERIALS AND METHODS

Synthesis and Characterization of Amphiphilic Molecules. The synthesis of AMP1-N and AMP1-B is based on a literature procedure[8] except that the diamine π-conjugated cores were reacted in a statistical reaction with the two acyl chloride wedges (polar and apolar).[30,32] The details of the synthetic procedure are given in the Supporting Information together with ^{1}H and ^{13}C NMR and MALDI TOF mass spectrometry characterization data.

Preparation of Nanoparticles. AMP1-N, AMP1-B, or a mixture of the two were dissolved in tetrahydrofuran (THF) at a concentration of 10^{-3} mol/L. To induce nanoparticle formation, 15 μL of such solution was injected quickly (*i.e.*, in 1−2 s) into 5 mL of ultrapure water, followed by a vigorous shake of the sample. The sample solutions were illuminated with a UV LED (emission wavelength of ~400 nm) to confirm that small nanoparticles formed (*i.e.*, no large aggregated clusters were present). Samples with low AMP1-B acceptor concentrations were obtained by successive dilution of an AMP1-N:AMP1-B blend solution in THF with solution containing only AMP1-N donor.

Characterization of Nanoparticles. Dynamic light scattering experiments were performed on an ALVCGS-3 compact goniometer, in the angular range 25−151°. The incident beam was produced by a HeNe laser operating at 532 nm. The intensity signal was sent to an ALV5000 digital correlator, using a typical acquisition time of 100 s for each angle. The calculation of the particle size distribution was performed using cumulant analysis. The DLS data were fitted to a first-order exponential decay, and from the extracted decay rates Γ the diffusion constant was determined and hydrodynamic radii obtained by making use of the Stokes−Einstein relation. Visualization by transmission electron microscopy was done with a Technai G2 Sphera by FEI, working at a voltage of 200 kV on a CCD chip of 1024 × 1024 pixels. Samples were prepared by drop-casting a 3 μM solution of nanoparticles on a carbon film on a 400 square mesh copper grid for 2 min. Small-angle X-ray scattering measurements were performed at the Dutch-Belgian BM26B beamline at the ESRF in Grenoble (France). An X-ray photon energy of 10 keV and sample-to-detector distance of 7 m were used, which allows a q-range of 0.05 $nm^{-1} < q < 0.9$ nm^{-1}, where q is the momentum transfer vector related to the angle of incidence (θ) and wavelength (λ) of the X-ray as $q = (4\pi/\lambda)\sin(\theta/2)$. At the sample position, the collimated beam was focused with a typical cross section of 0.1 × 0.3 mm^2. The SAXS images were recorded using a 2D multiwire gas-filled detector. The positions of diffracted peaks from standard silver behenate and rat tail collagen samples were used in order to calibrate the experimental q-range. The sample solutions were contained in 1 mm borosilicate capillaries. Standard data reduction procedures, *i.e.*, subtraction of the empty capillary contribution, correction for the solvent absorption and dark current, *etc.*, were applied.

Photoluminescence (PL) Spectroscopy. Time-resolved photoluminescence decay traces were taken using a Becker & Hickl time-correlated single photon counting module. Sample excitation was carried out at a wavelength of 375 nm, where the absorption for donor AMP1-N molecules is significantly stronger than that of AMP1-B (see Supporting Information). Excitation pulses were the frequency-doubled output of a mode-locked Ti:Sapphire laser. The photoluminescence emitted from the sample was collated, dispersed in a monochromator, and detected with a nitrogen-cooled charge-coupled device for time-integrated PL and a Peltier-cooled photomultiplier tube for time-resolved PL measurements. The full experimental setup has been described in detail elsewhere.[63,64] All measurements were performed in a linear regime with the excitation power (50 μW on a 200 μm spot diameter) and collection time chosen to avoid sample degradation.

Conflict of Interest: The authors declare no competing financial interest.

Acknowledgment. The authors acknowledge funding support from the Engineering and Physical Sciences Research Council and from The Netherland's Foundation for Scientific Reserach (NWO) through a VICI grant.

Supporting Information Available: Synthesis and characterization details for AMP1-N and AMP1-B molecules. Characterization data for AMP1-B nanoparticles (DLS, TEM, SAXS, UV−vis absorption). Circular dichroism spectra for the nanoparticles. Time-resolved photoluminescence decay traces measured at the acceptor emission wavelength. Plot of donor emission quenching *versus* acceptor concentration in nanoparticles. Dimensionality of energy transfer in the nanoparticle system explored with a KWW plot. This material is available free of charge *via* the Internet at http://pubs.acs.org.

REFERENCES AND NOTES

1. Kaeser, A.; Schenning, A. P. H. J. Fluorescent Nanoparticles Based on Self-Assembled *pi*-Conjugated Systems. *Adv. Mater.* **2010**, *22*, 2985–2997.
2. Howes, P.; Green, M.; Bowers, A.; Parker, D.; Varma, G.; Kallumadil, M.; Hughes, M.; Warley, A.; Brain, A.; Botnar, R. Magnetic Conjugated Polymer Nanoparticles as Bimodal Imaging Agents. *J. Am. Chem. Soc.* **2010**, *132*, 9833–9842.
3. Wu, C. F.; Bull, B.; Christensen, K.; McNeill, J. Ratiometric Single-Nanoparticle Oxygen Sensors for Biological Imaging. *Angew. Chem., Int. Ed.* **2009**, *48*, 2741–2745.
4. Zupke, O.; Distler, E.; Baumann, D.; Strand, D.; Meyer, R. G.; Landfester, K.; Herr, W.; Mailänder, V. Preservation of Dendritic Cell Function upon Labeling with Amino Functionalized Polymeric Nanoparticles. *Biomaterials* **2010**, *31*, 7086–7095.
5. Rahim, N. A. A.; McDaniel, W.; Bardon, K.; Srinivasan, S.; Vickerman, V.; So, P. T. C.; Moon, J. H. Conjugated Polymer Nanoparticles for Two-Photon Imaging of Endothelial Cells in a Tissue Model. *Adv. Mater.* **2009**, *21*, 3492–3497.
6. Bhongale, C. J.; Hsu, C. S. Emission Enhancement by Formation of Aggregates in Hybrid Chromophoric Surfactant Amphiphile/Silica Nanocomposites. *Angew. Chem., Int. Ed.* **2006**, *45*, 1404–1408.
7. Ishow, E.; Brosseau, A.; Clavier, G.; Nakatani, K.; Tauc, P.; Fiorini-Debuisschert, C.; Neveu, S.; Sandre, O.; Léaustic, A. Multicolor Emission of Small Molecule-Based Amorphous Thin Films and Nanoparticles with a Single Excitation Wavelength. *Chem. Mater.* **2008**, *20*, 6597–6599.
8. Petkau, K.; Kaeser, A.; Fischer, I.; Brunsverld, L.; Schenning, A. P. H. J. Pre- and Postfunctionalized Self-Assembled π-Conjugated Fluorescent Organic Nanoparticles for Dual Targeting. *J. Am. Chem. Soc.* **2011**, *133*, 17063.
9. Wu, C. F.; Szymanski, C.; Cain, Z.; McNeill, J. Conjugated Polymer Dots for Multiphoton Fluorescence Imaging. *J. Am. Chem. Soc.* **2007**, *129*, 12904–12905.
10. Yu, J. B.; Wu, C. F.; Sahu, S. P.; Fernando, L. P.; Szymanski, C.; McNeill, J. Nanoscale 3D Tracking with Conjugated Polymer Nanoparticles. *J. Am. Chem. Soc.* **2009**, *131*, 18410–18414.
11. Li, K.; Pan, J.; Feng, S. S.; Wu, A. W.; Pu, K. Y.; Liu, Y. T.; Liu, B. Generic Strategy of Preparing Fluorescent Conjugated-Polymer-Loaded Poly(DL-lactide-*co*-glycolide) Nanoparticles for Targeted Cell Imaging. *Adv. Funct. Mater.* **2009**, *19*, 3535–3542.
12. Chan, Y. H.; Wu, C. F.; Ye, F. M.; Jin, Y. H.; Smith, P. B.; Chiu, D. T. Development of Ultrabright Semiconducting

Polymer Dots for Ratiometric pH Sensing. *Anal. Chem.* **2011**, *83*, 1448–1455.
13. Kaeser, A.; Fischer, I.; Abbel, R.; Besenius, P.; Dasgupta, D.; Gillissen, M. A. J.; Portale, G.; Stevens, A. L.; Herz, L. M.; Schenning, A. P. H. J. Manuscript submitted for publication.
14. Abbel, R.; Schenning, A. P. H. J.; Meijer, E. W. Molecular Weight Optimum in the Mesoscopic Order of Chiral Fluorene (Co)polymer Films. *Macromolecules* **2008**, *41*, 7497–7504.
15. Zhang, X.; Chen, Z. J.; Würthner, F. Morphology Control of Fluorescent Nanoaggregates by Co-self-assembly of Wedge- and Dumbbell-Shaped Amphiphilic Perylene Bisimides. *J. Am. Chem. Soc.* **2007**, *129*, 4886–4887.
16. Antony, M. J.; Jayakannan, M. Molecular Template Approach for Evolution of Conducting Polymer Nanostructures: Tracing the Role of Morphology on Conductivity and Solid State Ordering. *J. Phys. Chem. B* **2010**, *114*, 1314–1324.
17. Zhang, X.; Rehm, S.; Safont-Sempere, M. M.; Würthner, F. Vesicular Perylene Dye Nanocapsules as Supramolecular Fluorescent pH Sensor Systems. *Nat. Chem.* **2009**, *1*, 623–629.
18. Förster, T. Experimentelle und theoretische Untersuchung des zwischenmolekularen Ubergangs von Elektronenanregungsenergie. *Z. Naturforsch.* **1949**, *4a*, 321.
19. Förster, T. H. 10th Spiers Memorial Lecture. Transfer Mechanisms of Electronic Excitation. *Discuss. Faraday Soc.* **1959**, *27*, 7–17.
20. Pope, M.; Swenberg, C. E. *Electronic Processes in Organic Crystals and Polymers*, 2nd ed.; Oxford University Press: New York, 1999.
21. Agranovich, V. M.; Galanin, M. D. *Electronic Excitation Energy Transfer in Condensed Matter*; North Holland Pub. Co.: Amsterdam, 1982; Vol. 3.
22. Wu, C. F.; Zheng, Y. L.; Szymanski, C.; McNeill, J. Energy Transfer in a Nanoscale Multichromophoric System: Fluorescent Dye-Doped Conjugated Polymer Nanoparticles. *J. Phys. Chem. C* **2008**, *112*, 1772–1781.
23. Herz, L. M.; Silva, C.; Friend, R. H.; Phillips, R. T.; Setayesh, S.; Becker, S.; Marsitsky, D.; Müllen, K. Effects of Aggregation on the Excitation Transfer in Perylene-End-Capped Polyindenofluorene Studied by Time-Resolved Photoluminescence Spectroscopy. *Phys. Rev. B* **2001**, *64*, 195203.
24. Qi, H. X.; Li, G. Q.; Mao, W. Y.; Wang, Q. S.; Zhu, T.; Li, G. W. Fluorescence Resonance Energy Transfer Mediated by Vesicles Containing Naphthalene Moiety. *Dyes Pigm.* **2007**, *74*, 454–457.
25. Wang, F. K.; Bazan, G. C. Aggregation-Mediated Optical Properties of pH-Responsive Anionic Conjugated Polyelectrolytes. *J. Am. Chem. Soc.* **2006**, *128*, 15786–15792.
26. Langhals, H.; Esterbauer, A. J.; Walter, A.; Riedle, E.; Pugliesi, I. Förster Resonant Energy Transfer in Orthogonally Arranged Chromophores. *J. Am. Chem. Soc.* **2010**, *132*, 16777–16782.
27. Abbel, R.; Schenning, A. P. H. J.; Meijer, E. W. Fluorene-Based Materials and their Supramolecular Properties. *J. Polym. Sci., Polym. Chem.* **2009**, *47*, 4215–4233.
28. Abbel, R.; Woffs, M.; Bovee, R. A. A.; van Dongen, J. L. J.; Lou, X.; Henze, O.; Feast, W. J.; Meijer, E. W.; Schenning, A. P. H. J. Side-Chain Degradation of Ultrapure π-Conjugated Oligomers: Implications for Organic Electronics. *Adv. Mater.* **2009**, *21*, 597–602.
29. Wu, C. F.; Szymanski, C.; McNeill, J. Preparation and Encapsulation of Highly Fluorescent Conjugated Polymer Nanoparticles. *Langmuir* **2006**, *22*, 2956–2960.
30. Abbel, R.; van der Weegen, R.; Meijer, E. W.; Schenning, A. P. H. J. Multicolour Self-Assembled Particles of Fluorene-Based Bolaamphiphiles. *Chem. Commun.* **2009**, *0*, 1697–1699.
31. Schwartz, B. J. Conjugated Polymers as Molecular Materials: How Chain Conformation and Film Morphology Influence Energy Transfer and Interchain Interactions. *Annu. Rev. Phys. Chem.* **2003**, *54*, 141–172.
32. Abbel, R.; van der Weegen, R.; Pisula, W.; Surin, M.; Leclère, P.; Lazzaroni, R.; Meijer, E. W.; Schenning, A. P. H. J. Multicolour Self-Assembled Fluorene Co-oligomers: From Molecules to the Solid State *via* White-Light-Emitting Organogels. *Chem.—Eur. J.* **2009**, *15*, 9737–9746.
33. Wu, C. F.; Peng, H. S.; Jiang, Y. F.; McNeill, J. Energy Transfer Mediated Fluorescence from Blended Conjugated Polymer Nanoparticles. *J. Phys. Chem. B* **2006**, *110*, 14148–14154.
34. Chen, Q.; Liu, N.; Ying, L.; Yang, W.; Wu, H.; Xu, W.; Cao, Y. Novel White-Light-Emitting Polyfluorenes with Benzothiadiazole and Ir Complex on the Backbone. *Polymer* **2009**, *50*, 1430–1437.
35. Liu, X. Z.; Zhu, R.; Zhang, Y.; Liu, B.; Ramakrishna, S. Anionic Benzothiadiazole Containing Polyfluorene and Oligofluorene as Organic Sensitizers for Dye-Sensitized Solar Cells. *Chem. Commun.* **2008**, *0*, 3789–3791.
36. Wu, C. F.; McNeill, J. Swelling-Controlled Polymer Phase and Fluorescence Properties of Polyfluorene Nanoparticles. *Langmuir* **2008**, *24*, 5855–5861.
37. Shaw, P. E.; Ruseckas, A.; Samuel, I. D. W. Exciton Diffusion Measurements in Poly(3-hexylthiophene). *Adv. Mater.* **2008**, *20*, 3516–3520.
38. Scheblykin, I.; Zoriniants, G.; Hofkens, J.; De Feyter, S.; Van der Auweraer, M.; De Schryver, F. C. Photoluminescence Intensity Fluctuations and Electric-Field-Induced Photoluminescence Quenching in Individual Nanoclusters of Poly(phenylenevinylene). *ChemPhysChem* **2003**, *4*, 260.
39. Vanden Bout, D. A.; Yip, W.-T.; Hu, D.; Fu, D.-K.; Swager, T. M.; Barbara, P. F. Discrete Intensity Jumps and Intramolecular Electronic Energy Transfer in the Spectroscopy of Single Conjugated Polymer Molecules. *Science* **1997**, *277*, 1074.
40. Möbius, D.; Kuhn, H. Energy Transfer in Monolayers With Cyanine Dye Scheibe Aggregates. *J. Appl. Phys.* **1988**, *64*, 5138.
41. Sundström, V.; Gillbro, T.; Gadonas, R. A.; Piskarskas, A. Annihilation of Singlet Excitons in J Aggreagtes of Pseudoisocyanin (PIC) Studies by Pico- and Subpicosecond Spectroscopy. *J. Chem. Phys.* **1988**, *89*, 2754.
42. Lude, D. R. *CRC Handbook of Chemistry and Physics*; CRC Press, 2001.
43. Parkinson, P.; Aharon, E.; Chang, M. H.; Dosche, C.; Frey, G. L.; Köhler, A.; Herz, L. M. Dimensionality-Dependent Energy Transfer in Polymer-Intercalated SnS_2 Nanocomposites. *Phys. Rev. B* **2007**, *75*, 165206.
44. Colby, K. A.; Burdett, J. J.; Frisbee, R. F.; Zhu, L.; Dillon, R. J.; Bardeen, C. J. Electronic Energy Migration on Different Time Scales: Concentration Dependence of the Time-Resolved Anisotropy and Fluorescence Quenching of Lumogen Red in Poly(Methyl Methacrylate). *J. Phys. Chem. A* **2010**, *114*, 3471–3482.
45. Maksimov, M. Z.; Rozman, I. M. On the Energy Transfer in Rigid Solutions. *Opt. Spectrosc.* **1961**, *12*, 337–338.
46. Baumann, J.; Fayer, M. D. Excitation Transfer in Disordered Two-Dimensional and Anisotropic Three-Dimensional Systems: Effects of Spatial Geometry on Time-Resolved Observables. *J. Chem. Phys.* **1986**, *85*, 4087–4107.
47. List, E. J. W.; Creely, C.; Leising, G.; Schulte, N.; Schlüter, A. D.; Scherf, U.; Müllen, K.; Graupner, W. Excitation Energy Migration in Highly Emissive Semiconducting Polymers. *Chem. Phys. Lett.* **2000**, *325*, 132.
48. Scheblykin, I.; Lepnev, L. S.; Vitukhnovski, A. G.; Auweraer, M. V. Electroluminescence and Optical Proerties of Poly(Phenylenevinylene)/J-aggregate Composites. *J. Lumin.* **2001**, *94*, 461.
49. Herz, L. M.; Silva, C.; Grimsdale, A. C.; Müllen, K.; Phillips, R. T. Time-Dependent Energy Transfer Rates in a Conjugated Polymer Guest-Host System. *Phys. Rev. B* **2004**, *70*, 165207.
50. Hoeben, F. J. M.; Shklyarevskiy, I. O.; Pouderoijen, M. J.; Engelkamp, H.; Schenning, A. P. H. J.; Christianen, P. C. M.; Maan, J. C.; Meijer, E. W. Direct Visualization of Efficient Energy Transfer in Single Oligo(*p*-Phenylene Vinylene) Vesicles. *Angew. Chem., Int. Ed.* **2006**, *45*, 1232–1236.
51. De, S.; Girigoswami, A. Fluorescence Resonance Energy Transfer—a Spectroscopic Probe for Organized Surfactant Media. *J. Colloid Interface Sci.* **2004**, *271*, 485–495.
52. Huebner, C. F.; Roeder, R. D.; Foulger, S. H. Nanoparticle Electroluminescence: Controlling Emission Color Through

Förster Resonance Energy Transfer in Hybrid Particles. *Adv. Funct. Mater.* **2009**, *19*, 3604–3609.
53. Tseng, K.-P.; Fang, F.-C.; Shyue, J.-J.; Wong, K.-T.; Raffy, G.; Del Guerzo, A.; Bassani, D. M. Spontaneous Generation of Highly Emissive RGB Organic Nanospheres. *Angew. Chem., Int. Ed.* **2011**, *50*, 7032.
54. van Rijn, P.; Janeliunas, D.; Brizard, A. M. A.; Stuart, M. C. A.; Eelkema, R.; van Esch, J. H. Introduction of Curvature in Amphipathic Oligothiophenes for Defined Aggregate Formation. *Chem.—Eur. J.* **2010**, *16*, 13417–13428.
55. Clark, J.; Silva, C.; Friend, R. H.; Spano, F. C. Role of Intermolecular Coupling in the Photophysics of Disordered Organic Semiconductors: Aggregate Emission in Regioregular Polythiophene. *Phys. Rev. Lett.* **2007**, *98*, 206406.
56. Yang, X. C.; Lu, R.; Xue, P. C.; Li, B.; Xu, D. F.; Xu, T. H.; Zhao, Y. Y. Carbazole-Based Organogel as a Scaffold to Construct Energy Transfer Arrays with Controllable Fluorescence Emission. *Langmuir* **2008**, *24*, 13730–13735.
57. Kasha, M. Energy Transfer Mechanisms and the Molecular Exciton Model for Molecular Aggregates. *Radiat. Res.* **1963**, *20*, 55.
58. Kasha, M.; Rawls, H. R.; Ashraf El Bayoumi, M. The Exciton Model in Molecular Spectroscopy. *Pure Appl. Chem.* **1965**, *11*, 371–392.
59. Powell, R. C.; Soos, Z. G. Singlet Exciton Energy Transfer in Organic Solids. *J. Lumin.* **1975**, *11*, 1–45.
60. Blumen, A.; Manz, J. On the Concentration and Time Dependence of the Energy Transfer to Randomly Distributed Acceptors. *J. Chem. Phys.* **1979**, *71*, 4694–4702.
61. Beljonne, D.; Shuai, Z.; Pourtois, G.; Bredas, J. L. Spin-Orbit Coupling and Intersystem Crossing in Conjugated Polymers: a Configuration Interaction Description. *J. Phys. Chem. A* **2001**, *105*, 3899.
62. Ebbinghaus, S.; Kim, S. J.; Heyden, M.; Yu, X.; Heugen, U.; Gruebele, M.; Leitner, D. M.; Havenith, M. An Extended Dynamical Hydration Shell Around Proteins. *Proc. Natl. Acad. Sci. U. S. A.* **2007**, *104*, 20749–20752.
63. Stevens, A. L.; Janssen, P. G. A.; Ruiz-Carretero, A.; Surin, M.; Schenning, A. P. H. J.; Herz, L. M. Energy Transfer in Single-Stranded DNA-Templated Stacks of Naphthalene Chromophores. *J. Phys. Chem. C* **2011**, *115*, 10550–10560.
64. Chang, M. H.; Hoeben, F. J. M.; Jonkheijm, P.; Schenning, A. P. H. J.; Meijer, E. W.; Silva, C.; Herz, L. M. Influence of Mesoscopic Ordering on the Photoexcitation Transfer Dynamics in Supramolecular Assemblies of Oligo-*p*-Phenylenevinylene. *Chem. Phys. Lett.* **2006**, *418*, 196–201.